Experimental study of miscible displacement fronts in rough self-affine fractures

Harold Auradou* and Jean-Pierre Hulin
Laboratoire Fluide, Automatique et Systèmes Thermiques, UMR No. 7608, CNRS, Université Paris 6 and 11, Bâtiment 502, Université Paris Sud, 91405 Orsay Cedex, France

Stéphane Roux
Laboratoire ''Surface du Verre et Interfaces,'' UMR CNRS/Saint-Gobain, 39 Quai Lucien Lefranc, Boîte Postale 135, F-93303 Aubervilliers Cedex, France

(Received 10 January 2001; published 23 May 2001)

Miscible fluid displacements are studied experimentally in a radial flow between two complementary replica of a self-affine rough granite fracture surface. The displacement front between a dyed fluid and a transparent (but otherwise identical) one is followed optically through one face of the cell. The evolution of its geometry is studied as a function of time, flow-rate, and normal and lateral relative displacements between the two surfaces. For a purely normal displacement, the front is globally smooth, due to the constant local distance between surfaces. For a finite lateral displacement, the front is rough due to spatial variations of this distance; its geometry is fractal and its dimension is directly related to the Hurst exponent $H \approx 0.8$ of the surface. The fractal regime is observed only above a lower cut-off scale that depends on the normal spacing of the surfaces and an upper one that increases with the injected volume and with the amplitude of the lateral displacement.

DOI: 10.1103/PhysRevE.63.066306 PACS number(s): 47.55.Mh, 05.40.−a, 91.45.Vz, 47.53.+n

I. INTRODUCTION

The transport of fluids and dissolved contaminants in fractured rocks is of key interest for many practical applications such as soil and water pollution, oil and gas recovery and waste storage. Flow in fractured rocks is often characterized by the very broad distribution of the flow velocities and by strong heterogeneities of the flow field. Preferential flow paths naturally emerge and they influence strongly the geometry of the displacement fronts and often invalidate models based on effective homogeneous media approaches.

Flow heterogeneities are present both at the scale of the fracture network and at that of the individual fractures. In a network of fractures with a broad distribution of the apertures and/or with a low fracture density, fluids flow essentially through a small fraction of the fractures and hence only the latter subset controls solute transport [1–3].

In the present work, we analyze experimentally flow through a single fracture. Its geometry is modeled as the aperture between two perfectly matching rough surfaces translated with respect to each other with a controlled normal and lateral shift. We ignore elastic or plastic deformations that may occur in the bulk of the rock and invalidate the perfect matching hypothesis. As will be shown below, parallel plane models, assuming smooth flat fracture walls, do not indeed provide an adequate description of flow since they cannot account for preferential paths which are often observed. The roughness of the walls indeed induces local aperture fluctuations resulting in fluid velocity variations. These channeling effects have been studied both numerically and experimentally. In a first type of simulations [4–6], the full flow field is computed in the case of a two-dimensional (2D) flow between rough lines representing fracture profiles. This allows to analyze the influence of low velocity recesses inside deep grooves but not that of the disorder of a 2D distribution of local apertures. Adler and co-workers [7] report full 3D numerical simulations of tracer dispersion in rough fractures that demonstrate an increase of dispersion due to fracture roughness. Finally, tracer dispersion in flow between matching self-affine surfaces was analyzed in the lubrication approximation [8] as a function of the relative displacement of the two surfaces: it was shown that dispersion increases with the lateral displacement and decreases with the mean normal spacing. Moreover a theoretical analysis [9] of this problem taking into account the multiplicity of scales of self-affine fracture roughness showed that the displacement front should display a self-affine geometry related to that of the fracture surface. This result has been obtained using a perturbative approach from the simple parallel plane geometry; however, as discussed below this self-affine geometry for the front may expand to the stage of giving rise to a fractal geometry. This result gives some insight on the ''preferential channeling'' phenomenon, and motivates our experimental analysis of the front geometry.

On the other hand, laboratory experiments [10–13] using fracture surface replica or real fractures confirm that surface roughness has a strong influence on the flow distribution and on the variability of the transport properties. Small scale field experiments [14] in a granite quarry have also been reported. In this latter work, a single subvertical fracture is isolated between two vertical boreholes. Water is injected through a third oblique borehole intersecting the fracture. The analysis of the flow rate distribution between several sampling points distributed at the surface and in the lateral holes demonstrates the localization of the flow inside very few channels. Such flow heterogeneities in fractures are largely due to the

*Present address: Service de Physique et Chimie des Surfaces et Interfaces, Commissariat à l'Énergie Atomique, Bâtiment 462, 91191 Gif-sur-yvette Cedex, France. Email address: Harold.Auradou@cea.fr

geometry of the fracture walls that have a broad range of characteristic length scales; the velocity distribution also depends on the relative displacement of the complementary fracture surfaces. When these surfaces are just pulled apart perpendicular to their mean plane, the local fracture aperture remains constant (and the flow velocity varies slowly). On the contrary, when the two surfaces are displaced laterally, the local aperture becomes variable, inducing in turn strong spatial inhomogeneities of local flow velocity. This lateral displacement mimics fault slip effects that are very common in natural fractures.

The objective of the present work is to study the influence of the relative displacements of such fracture surfaces on the velocity distribution of a fluid flowing between them. Practically, heterogeneities of the velocity distribution can be inferred from the geometry of the displacement front of a transparent fluid by a miscible, dyed one of same density in a radial flow configuration. A particularly important issue concerns the front geometry that may give information on the number of channels and their size. The basic issue here is to study the characteristic scales that may occur in such a problem. Indeed, it has been frequently observed that the roughness of fracture surfaces is not confined to a narrow range of typical wavelength or asperity shapes. In contrast, such surfaces have been shown to obey a statistical scale invariance, known as self-affinity [15,16]. This description holds both for man made [17,18] and natural fractures [19,20] and for a broad variety of materials and length scales [21]. Such surfaces, assumed to be on average parallel to the (x,y) plane, are described here through a single valued function $z=h(x,y)$. The self-affinity property means that the surface remains statistically invariant under the scaling transformation

$$h(\lambda x,\lambda y)=\lambda^{H}h(x,y), \tag{1.1}$$

where the equal sign is to be understood in the statistical sense as giving rise to the same expectation value for any observable computed through an average over space. H is the characteristic roughness exponent called Hurst's exponent. Experimental values of H are close to 0.8 ± 0.05 for many materials such as granite but has been found to be close to 0.5 for sandstone [22]. Many experiments suggest that the roughness exponent is independent on the direction of the measurement in the mean fracture plane [23,13].

The observations of displacement fronts and flow channels reported here were performed on model fractures with one transparent face. The fracture surfaces are complementary casts of a same granite fractured surface. The topography of the casts is analyzed and shown to have long range correlations. We shall first describe the experimental setup and the procedure used to characterize the surfaces and analyze quantitatively the geometry of the displacement front of a fluid by another miscible dyed one. We shall then demonstrate that these fronts display a fractal geometry over a finite range of length scales with a characteristic exponent related directly to the self-affine exponent of the surface as expected from the above mentioned theoretical analysis [9]. We shall then analyze the dependence of the upper and lower bounds of the fractal domain on the experimental parameters (normal and lateral relative displacements of the surfaces, flow rate, injected volume).

II. EXPERIMENTAL SETUP AND PROCEDURE

A. Realization and characterization of experimental fracture samples

The experimental setup includes first a model fracture made of two complementary casts of a same fractured granite block. The granite blocks were of size $25\times25\times40$ cm^3 and obtained from a quarry in Lanhélin (Britanny). Two facing notches are carved parallel to the large square faces in the middle of two opposite smaller faces. They are then submitted to compressions of opposite direction by two sharp edges until a mode *I* [24] crack is propagated from one notch to the opposite.

Each surface is molded using a master silicone rubber (Rhone Poulenc RTV 573*A*). It is used in turn to cast a transparent epoxy replica (using Araldite 2020*A* and *B*) of the original fracture surface. We obtained with this procedure epoxy casts of all the fractured granite surfaces used in the experiments. In order to avoid the influence of the small deformations of the epoxy replica during the polymerization process (bending and stretching), the epoxy casts are again molded with the silicon rubber in order to obtain perfectly matching surfaces that are the model fractures used in the experiments. Before inserting these surfaces into the experimental setup, the topography of the epoxy casts is characterized by means of a mechanical profilometer. The rough interfaces are placed on a (x,y) translation table and translated by 250 μm between each height measurement. The local height is measured by lowering a stylus onto the rough surface and detecting the contact by a high resolution Renishaw sensor. The precision of the height measurement is roughly 10 μm. The topography is thus obtained on a square grid of 760 lines including 770 points each, with an equal spacing (250 μm) between points and lines. The roughness exponent is determined by computing the power spectral density $P(f)$ of the height variations $h(x)$ along each profile and averaging over a large enough number of profiles (a linear interpolation of the global variation of height between the end points of each profile is subtracted out [25]). For fully self-affine profiles, the Fourier spectrum scales with the spatial frequency like

$$P(f)\propto f^{-1-2H}. \tag{2.1}$$

Power spectra of profiles obtained, as described above, on moldings of fractured granite surfaces display indeed a power law behavior over a broad range of wave vectors corresponding to length scales ranging from a few 40 mm down to 0.75 mm. The corresponding Hurst exponents are

$$H=0.77\pm0.05 \tag{2.2}$$

and are the same for the two x and y directions. This implies that the fracture surface is isotropic from that point of view. These results confirm previous measurements on fractured granite surfaces [26,13,12]

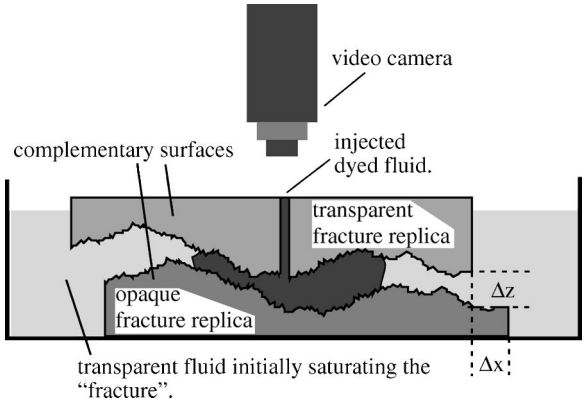

FIG. 1. Schematic view of the experimental fluid displacement measurement setup. The transparent fracture replica is fixed while the opaque replica can be moved down and horizontally.

B. Experimental setup

The model fracture is located inside a parallelepipedic basin initially filled with a transparent solution (See Fig. 1): the flat side of the silicon rubber molding is glued onto the bottom of the basin that can move vertically with an amplitude of 12 mm and in both horizontal directions with an amplitude of ± 25 mm. The rubber molding has been cut out to a circular shape with its center at the injection point. This allows to obtain an isotropic constant pressure boundary condition and to ensure that the outer boundary influences the flow distribution only over a small distance. The transparent epoxy cast is initially placed with its rough lower side in perfect contact with the mating complementary rubber surface. The optical index of the epoxy is close enough to that of the fluid so that the effect of index mismatch at the rough interface can be neglected. Moreover, the upper side is flat and covered with a fluid layer to reduce optical distortion due to topographic imperfections of its surface (residual roughness or undulations appearing during the polymerization process).

The epoxy cast is held in a square metal frame: sideways motion is blocked by ball point devices adjusted when both surfaces are initially in contact. A propping device is also adjusted initially to prevent downward displacements of the upper surface. After this initial positioning, the upper fracture surface can only move upward from its initial position at which the two surfaces are in contact. Several micrometric sensors allow to detect upward motions and check that the amplitude of sideways displacements remain within the allowed limits (typically $\pm 15\ \mu m$). In the preparation stage, the basin and the fracture moldings are first fully saturated with a transparent solution in such a way that no trapped bubbles remain within the fracture that could affect the flow.

The dyed solution is then injected through a small borehole at the middle of the upper epoxy cast. The transparent solution is a mixture of 10% of glycerol, 90% in weight of water and 0.2 g/l of NaCl. The dyed solution is identical save for NaCl that is replaced by nigrosine. The densities of the solutions are measured with a (Altan Paar DMA 35N) densimeter and found equal to $\rho = 1.0231 \pm 2 \times 10^{-4}$ g/cm^3 at 19.5 °C. Significant distortions of the invasion front geometry are observed when the densities of the injected and displaced solutions are not exactly equal. The two solutions must, in particular, be kept at the same temperature since a temperature variation of 2 °C induces a density variation of 10^{-3} g/cm^3. In order to reduce this effect, the transparent liquid in the basin and the dyed solution are stored at the same temperature and their densities are checked to be equal before each experiment. For all the experiments reported here the density difference between the two solutions is lower than 25×10^{-4} while their viscosity is 1.288 cP at 20 °C [27]. Separate syringe pumps are used to handle the two fluids and are run simultaneously: a low volume valve allows to switch the injection from one solution to the other without stopping the flow. The cell is uniformly illuminated from above by four halogen lamps placed around the setup. Pictures of the dye invasion front are realized by a high resolution cooled (CCD) video camera placed above the fracture and providing 1300×1030 pixel images with 4096 gray levels. The corresponding spatial resolution is 250 μm in both directions.

C. Experimental fluid injection and image analysis procedure

A steady radial flow of the transparent fluid is first established in the model fracture and a reference image of the initial state of the fracture is recorded; then, the injection valve is quickly switched to start the injection of dyed fluid and the output of the CCD camera is saved at constant time intervals. Between 10 and 20 images are obtained during each injection run. After the end of an experiment, the dyed solution is sucked back through the injection hole before a new injection is begun. Experimental parameters (flow rate, injection time or relative displacement of the surfaces) may therefore be changed between two experiments without having to take the setup apart. Figure 2 displays typical sample images obtained during two such experiments. In spite of the small thickness of the fluid layer (0.5 mm to 1.5 mm) and of the low dye concentration, the optical density of the dyed fluid is quite high: thus, the boundary between the invaded region and the area remaining fully saturated with transparent fluid is clearly visible. In order to reduce the effect of reflectivity variations of the lower surface, each image is divided pixel by pixel by the reference one (obtained before the invasion has begun). The resulting gray levels are nearly constant in the noninvaded zone that further enhances its contrast with the invaded regions.

The fluid displacement is not fully bidimensional due to the Poiseuille velocity profile between the rough surfaces: the dye moves indeed faster midway between these surfaces than near both of them. At high flow rates, the front outer contour is determined by this fast moving fluid. It is however well defined since the velocity profile is extremal in this zone and the thickness of dyed fluid near the front is large enough to allow for an easy detection. At low flow rates, transverse molecular diffusion homogenizes the tracer distribution across the aperture. The resulting process corresponds to the well-known Taylor mechanism [28]: it broadens the concentration front following a convection diffusion equation characterized by a dispersion coefficient proportional to the square of the velocity.

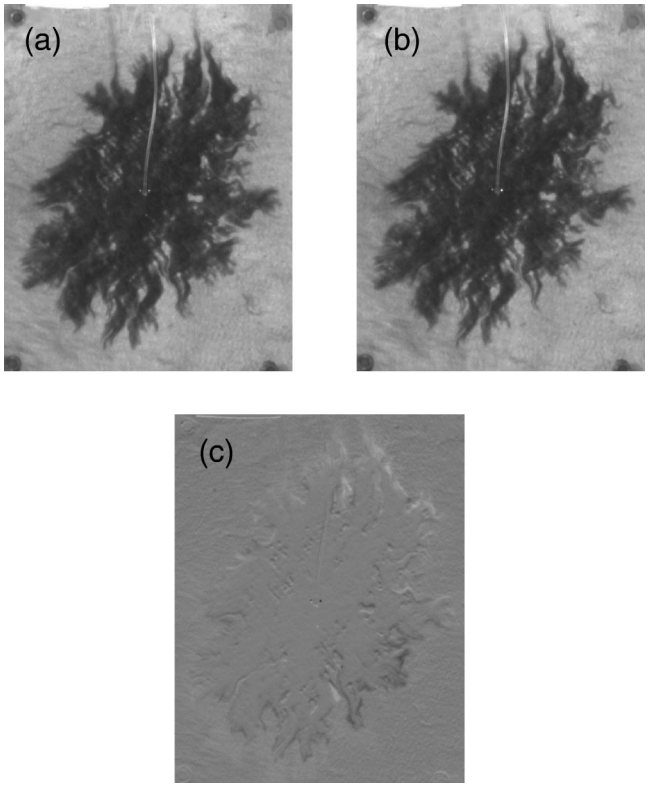

FIG. 2. Compared invasion fronts observed at two different injection flow rates Q for same normal ($h=1$ mm) and lateral ($u=3.70$ mm) displacements between complementary surfaces. (a) $Q=1.12$ ml/min, (b) $Q=13.5$ ml/min, (c) difference between images (a) and (b). The image size is 22×17 cm^2.

Experimentally, the front contour is determined by a binary thresholding procedure. We first compute an histogram of the gray levels in the normalized image where noninvaded zones correspond to a sharp peak in gray levels whereas invaded ones are much more broadly distributed. A binary image is obtained by thresholding the gray levels at a value equal to the lower value of the noninvaded gray level peak. A manual correction is then performed to eliminate irrelevant isolated ''invaded'' pixels due to noise outside the invasion front. The invasion front is finally defined as the outside ''contour'' of the binarized and corrected invaded zone. The relevance of this procedure is controlled visually by superimposing the computed front and the original normalized image as shown in Fig. 3. This allows to check that the geometrical features of the front are correctly captured and that no artificial structures are introduced.

III. EXPERIMENTAL RESULTS

A. Qualitative dependence of front geometry on experimental control parameters

Two different model samples, both corresponding to fractured granite surfaces, have been tested. We studied the influence of the following parameters: injection flow rate, normal relative displacement h with respect to the contact position (representing the average of the local apertures over the surface), lateral relative displacement u. In order to obtain these informations, several series of experimental runs have been performed in which one of these experimental parameters was kept constant and the other ones were varied.

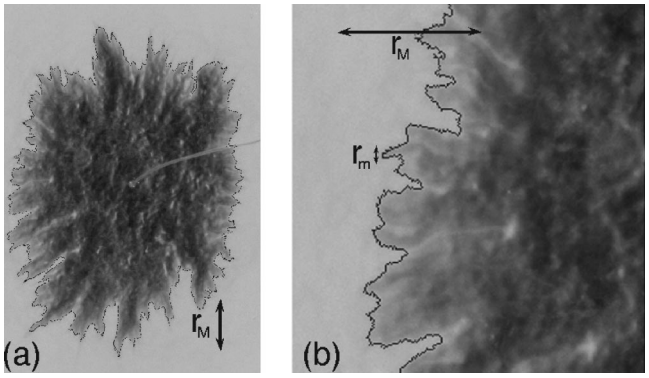

FIG. 3. Superposition of normalized image of injected fluid and of displacement contour determined by binary thresholding procedure. (a) global view of invaded zone. (b) detailed view of a part of the front. The experimental conditions were $Q=3.3$ ml/min, $h=0.5$ mm, and $u=1.2$ mm. The dimension of the pictures is for (a) 190 mm$\times$142 mm and for (b) 62 mm$\times$62 mm. The two limiting lengths of the fractal domain $r_m=1.5$ mm and $r_M=25$ mm are indicated on the views.

The first important point, conditioning our further analysis, is to study the influence of the flow rate on the front geometry. As already pointed above, the concentration distribution of tracer (here dye) during the injection is determined by several mechanisms [9]. The most relevant to our experiment is geometric dispersion due to the inhomogeneous velocity induced by the spatial distribution of aperture. Molecular diffusion (parallel and transverse to the flow) and Taylor dispersion due to the local parabolic velocity profile between the two rough surfaces may also play a part, however they are expected to control, respectively, much slower or faster flows. Since these mechanisms depend in a different way on the flow velocity, the invasion front geometry will be determined by the dominant mechanism.

One observes in Figs. 2(a)-(b) that invasion fronts obtained at two different flow rates in a ratio of 1 to 15, but with an identical injected volume, are practically indistinguishable. Figure 2(c) displays the difference between the two images (a) and (b): its nearly constant gray level proves that the front geometries are identical within a good precision. This implies that, in this range of flow velocities, geometric dispersion is the dominant effect since it is the only mechanism for which the front geometry is independent of velocity for a fixed injected volume of fluid [spreading due to Taylor dispersion (high velocities) increases with velocity and that due to molecular diffusion (low velocities) decreases].

Even in the above range of velocities the parabolic velocity profile in the interval between the rough surfaces may however influence the 3D spatial distribution of the dye. At the lower velocities, its spreading effect is balanced by transverse molecular diffusion resulting in Taylor dispersion — estimated to have a small contribution in that case. At higher velocities, transverse molecular diffusion is too slow to influence significantly the dye distribution along its path. Then,

as already pointed above, the front boundary corresponds to fast moving fluid half way between the walls (even if slow moving dye near the walls is left behind). The outer boundary has thus the same geometry as at lower flow rates where the front spreads out at the mean velocity (the ratio between the two is 3/2 at a given flow rate).

At still higher velocities beyond the range discussed above, the Reynolds number may be larger than 1 and front geometry variations due to changes in the flow distribution may occur. At the other end, at very low velocities (experiments lasting for a day or more) the invaded zone drifts sideways towards one of the boundaries. This may be due to residual density differences between the two solutions and to the imperfect horizontality of the model.

In conclusion, the front boundary geometry is invariant over a significant range of flow velocities (Fig. 2): it is determined in that range essentially by the 2D geometrical disorder of the velocity field in the mean fracture plane (either the average of the local velocity over the interval between the surfaces or the maximum velocity inside it). Other measurements such as that of transit time distributions would on the contrary be influenced by the 3D distribution of the tracer (in particular by slow moving fluid near the walls). We concentrate in the following our study on the dependence of the front geometry on the relative position of the two surfaces and on the injected volume at flow-rates from 1.12 ml/min to 13.5 ml/min.

A key parameter controlling the disorder of the flow field is the lateral displacement u. Figure 4 compares the shape of the invasion fronts observed for a same normal displacement $h=0.5$ mm of the surfaces and a same flow-rate Q with zero and nonzero values of u. The two geometries are clearly markedly different: when no lateral shift is introduced, Fig. 4(a), the contour of the invaded zone is as expected smooth and regular. Fine radial striations perpendicular to the front are however observed near the edge. Their origin is not completely known but the most likely explanation is the small aperture variations due to the local slope of the surfaces [5]. While the vertical distance between surfaces is constant, the effective aperture for the fluid flow (perpendicular to its mean velocity) varies. The ratio between the two corresponds to the cosine of the angle of the mean velocity with respect to horizontal.

A second explanation is small roll-like gravitational instabilities already observed by other authors [29] in similar geometries. These are associated with gravitationally unstable stratifications created near the front by the velocity profile in the space between surfaces; their occurrence requires a nonzero density contrast between the fluids — a rather unlikely occurrence in view of our experimental procedure. Observed deviations of the outer contour from a perfect circular shape were also to be expected due to unavoidable imperfections of the castings and of the angular alignment of the surfaces.

For the same normal displacement $h=0.5$ mm and a lateral displacement $u=1.2$ mm (Fig. 4), the surfaces almost touch each other and the local distance between them varies significantly from point to point. Fingers appear at very different scales. This reflects the strong influence of local thickness variations on the spatial flow distribution and the appearance of preferential flow channels of sizable width. Small light zones are also observed within the dark invaded region: they correspond to points of reduced local thickness where the flow velocity is very low and dye has to move in and out only through molecular diffusion.

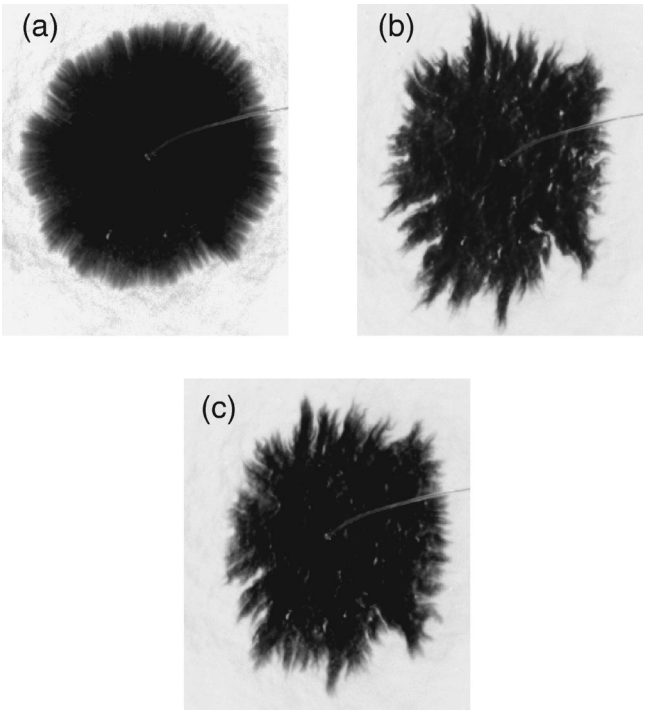

FIG. 4. Compared invasion fronts observed for a same injection flow rate ($Q=3.3$ ml/min) and a same normal displacement ($h=0.5$ mm) and for zero and nonzero lateral displacements u between complementary rough surfaces. (a) $u=0$ mm, (b) $u=1.2$ mm, (c) $u=0.5$ mm. All the pictures have a dimension of 190 mm$\times$160 mm.

For a smaller lateral displacement ($u=0.5$ mm), but the same mean aperture $h=0.5$ mm [Fig. 4(c)], many features of the invasion front are visible at the same location than in Fig. 4(b) but have a reduced amplitude parallel to the mean flow direction. This implies that velocity contrasts that create them are smaller than for $u=1.2$ mm, reflecting the narrower distribution of local aperture variations.

Experiments have been also been performed for several different mean normal spacings h and a fixed lateral displacement u. In such cases, the absolute values of the local thickness fluctuations remain the same but their relative values decrease as h increases. Figure 5 shows the comparison of images obtained for two such experiments with h, respectively, equal to 1.25 and 1.75 mm. While the largest structures remain at the same location, the interface appears smoother for the largest value of h and many small geometrical features of the front are not visible for $h=1.75$ mm. In addition, inside the invaded region, one sees fewer light colored zones where dye has not penetrated due to a very low local velocity.

B. Expected front geometry

As developed in the introduction, it is important to characterize the channeling of flow in fractures, and the morphol-

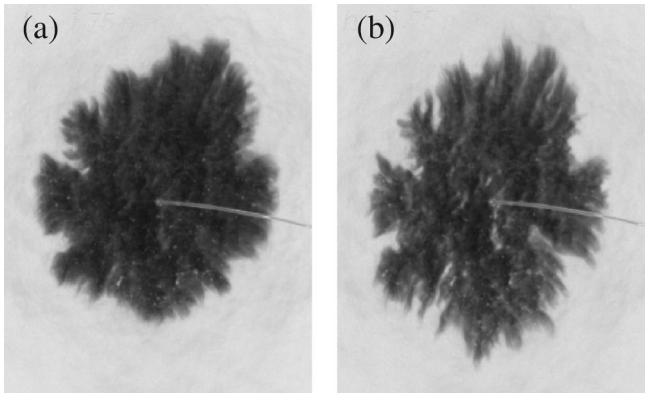

FIG. 5. Compared invasion fronts observed for a same injection flow rate ($Q=6.45$ ml/min) and a same lateral displacement ($u=2$ mm) but with different mean normal displacements between the two surfaces. (a) $h=1.75$ mm (b) $h=1.25$ mm. The images have the same size 190 mm$\times$150 mm and the area covered by the dyed fluid is the same in both pictures.

ogy of the tracer front is a direct indication of this phenomenon. The above presented experimental images show, in a qualitative fashion, that the front displays a tortuous geometry with multiple characteristic length scales. Moreover, a theoretical analysis of this situation in the geometric dispersion regime (but in a parallel flow geometry) showed [9] that, starting from a straight geometry, the tracer front would progressively develop of self-affine geometry with a roughness exponent H_f such that

$$H_f=H. \tag{3.1}$$

The self-affine geometry description is valid between a lower and an upper cut-off scale ℓ_m and ℓ_M. The lower scale is of order the larger distance between h or u, whereas the upper scale increases with the traveled distance up to the stage where it reaches the system size and saturates. Similarly, the amplitude of the front deviation increases with the advection distance. Although these results are based on a perturbative treatment of the aperture fluctuations, their validity is not restricted to small front roughness nor even small slopes. This is quite unusual since, generally, when a rough front or surface reaches locally slopes of order unity, novel physical effects comes into play, and invalidate the small scale description. In our case, we may tolerate arbitrarily large slopes of the front as compared to its mean orientation and still trust the theoretical analysis. A consequence of this is that it may be convenient to characterize the self-affinity of the front using tools developed for the determination of fractal dimensions.

It must be remembered that the fractal dimension of a self-affine function is not uniquely defined. The result depends on the method used and on the range of scales considered. It is convenient to introduce the ''topothesy'' or the scale at which the slope of the function is of order unity. Above the topothesy, the fractal dimension is trivially equal to the topological dimension, i.e. 1 for a front, 2 for a surface. At smaller length scales, the dimension can assume nontrivial values. In particular for the box-counting method, the dimension is found to be $D=d-H$ where d is the embedding space dimension. Because of the fact that the topothesy is generally smaller or equal to the lower cutoff, such methods generally do not constitute a practical way of measuring the self-affine exponent, and other methods (such as the power spectrum) are more appropriate. In our case, this approach should be convenient since the fronts display structures of sizable length parallel to the flow. The expected fractal dimension of the front should be $D=2-H_f=2-H\approx 1.2$.

The main difference between the theoretical modeling and the experiment presented in this paper is the parallel flow geometry in the former case, compared to the radial flow in the latter. Radial flow implies a systematic decrease of the fluid velocity as a function of the distance from the injection point. However, this effect is expected to have no major consequence since, in the geometric dispersion regime, only the injected volume matters and not the absolute velocity. The lower cutoff should remain unaffected. The Hurst exponent of the self-affine regime should still hold at small scales. A systematic curvature of the front is also expected a large scales (due to the circular shape of the front on average). This may introduce an upper cutoff proportional to the radius of the front. However, the upper cutoff of the parallel flow regime should also be present and still scale as the distance traveled by the front, or again as the radius itself. Therefore, we do expect that the upper scale should vary as the square root of the injected volume (or time) irrespective of the limiting phenomenon.

C. Quantitative analysis of the fractal external front geometry

Following this theoretical expectation, we shall analyze now whether experimental invasion front geometries can be considered as fractal and over which range of length scales. The average mass method has been selected [15] to identify the fractal characteristics of these fronts and their dependence on the experimental control parameters. A few tests have been performed on the same set of images using the box counting technique: they gave results very similar to those of the average mass approach and will not be presented here.

Let us label by an index i pixels located on the external contour of the front. The number of such pixels $N_i(r)$ located at a distance smaller than r from an origin site i (belonging to the front) is first computed. The average of $N_i(r)$ over all sites i provides $\langle N(r)\rangle$ that is displayed in Fig. 6(a) using a log-log scale. For a fractal contour, $N(r)$ should increase with r following a power law, $N(r)\propto r^D$ where $1\leqslant D\leqslant 2$ is the fractal dimension. ($D=1$ would correspond to a smooth Euclidian line and $D=2$ to a tortuous contour filling completely the plane).

One observes in Fig. 6(a) that a single straight line cannot account for $N(r)$ variations at all r values. The center part of the curve can be fitted with a straight line of slope 1.26 while a slope 1 provides a better fit on both sides of that range (the large deviations on the right correspond to distances of the order of magnitude of the global size of the invaded zone). In order to observe more clearly the different domains, the

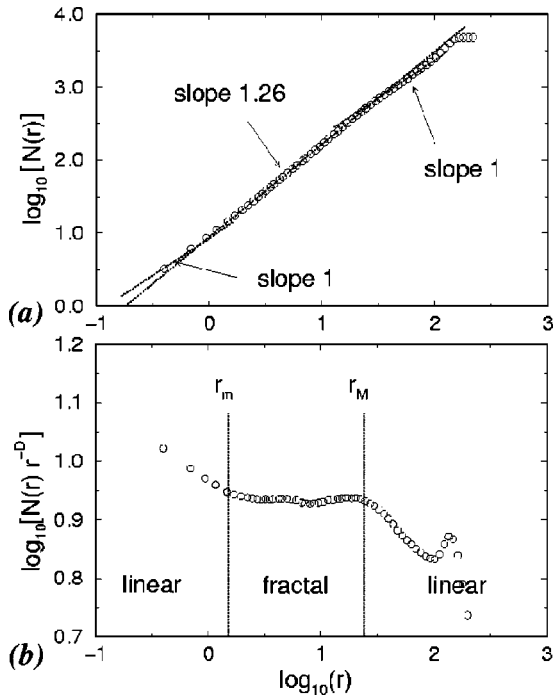

FIG. 6. (a) Average variation of the number $N(r)$ of pixels located on the invasion front shown in Fig. 3 within a distance r (in mm) of an origin pixel on the front. The dotted line (slope 1.26) represents a variation of $N(r)$ proportional to $r^{1.26}$ representing the expected dependence of $N(r)$ on r for a fractal front of dimension $D=1.26$. (b) Variation with the distance r of $N(r)r^{-D}$ with $D=1.26$ for the same experiment as in Fig. 6(a).

variation of $N(r)r^{-D}$ is plotted in Fig. 6(b) as a function of r for $D=1.26$. A fractal curve of dimension D would give indeed a straight horizontal line at all length scales so that this type of plot will be used systematically in the following. As expected, the curve is horizontal in the center part corresponding to the fractal domain and deviations are observed on both sides where $N(r)$ varies roughly linearly with r. We conclude that the outer contour of the invasion front is fractal and (in the present case) of dimension $D=1.26$ between two limiting length scales r_m and r_M, respectively, of the order of 1.5 mm and 25 mm. These two values correspond qualitatively well to the typical size of the smallest and largest features visible in the front shown in Fig. 3(b). At smaller and larger distances, the front behaves as an Euclidian curve of characteristic dimension 1. However, it was not possible to subtract out this large scale global Euclidian shape in order to map the front onto a linear profile. The global shape is not circular because of the anisotropy induced by the displacement ([8]) and could not be modeled as a simple geometry.

The fractal analysis of the front appears therefore as an appropriate tool to characterize the invasion front; however, some parts of the front displayed in Fig. 3 differ visually from others. This appears clearly when one compares the bottom part of the front that displays well developed structures and its right part that seems smoother. To see if the fractal dimension characterize the whole structure of the front or only a part of it, we computed the fractal dimension

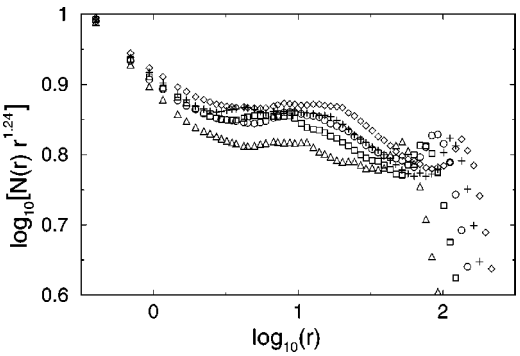

FIG. 7. Variation as a function of distance r (in mm) of $N(r)r^{-D}$ with $D=1.24$ at different injection times during a same experiment performed at a flow rate $Q=6.45$ ml/min for a fixed relative position of the two fracture surfaces $u=2$ mm and for a fixed mean normal spacing $h=1.25$ mm. ($\diamond$)$t=180$ s; ($+$)$t=130$ s; ($\bigcirc$)$t=80$ s; ($\square$)$t=55$ s; ($\triangle$)$t=30$ s.

of different parts of the fronts. As example, the front shown in Fig. 3(a) was cut in four sections of equal size corresponding, respectively, to the top, the right, the bottom, and the left parts of the front. The fractal dimension of the bottom and left parts were found to be 1.26 as measured when the entire front is considered. The dimension of the two other parts were only sightly different: 1.29 for the top part and 1.23 for the left part. Moreover, the lower cutoff r_m of the fractal domain was the same for all four sections. On the other hand, the two sections differed markedly through the value of the upper limiting length r_M of the fractal domain: r_M reflects the maximum size of the structures and is greater in the top of the front than at its left . This result indicates that the fractal dimension characterizes the entire multiscale structure of the front. The same result is also obtained on other experiments and the deviation of local dimension values is of order ± 0.03.

Although these results agree nicely with theoretical expectations, they must be regarded with caution since the width of the fractal regime corresponds only to a range of length scales of about one decade. Therefore, in order to establish more firmly this result, we have tested the robustness of the value of D as a function of the injected volume (or of time since the flow rate is constant) and for different values of the parameters u and h. Moreover, in all this part of the study, quantitative analysis is performed only on invasion fronts for which less than two-thirds of the model surface is filled with the invading fluid. This allows to avoid further the influence of the constant pressure outer boundary that is already limited to a minimum by its circular shape.

1. Dependence on the injected volume

For a fixed relative displacement (h and u) between the two rough walls, we studied the dependence of the fractal regime on the injected volume. As can be seen in Fig. 7 corresponding to injection times ranging between 30 and 180 s, the fractal dimension D remains constant within ± 0.02 during the injection. In this experiment, the best fit at intermediate distances was obtained for $D=1.24$ (the same value was used for all curves). In the set of curves of Fig. 7, the

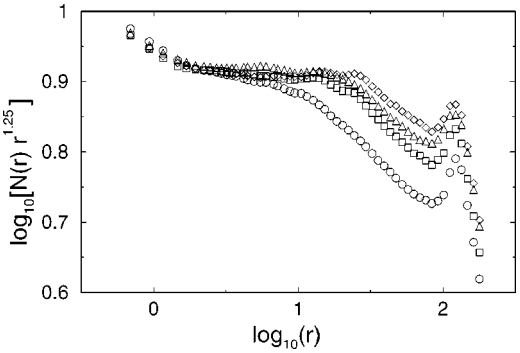

FIG. 8. Variation with the distance r (in mm) of $N(r)r^{-D}$ with $D=1.25$ for a series of experiments performed at a same flow rate $Q=3.3$ ml/min and for a same mean normal spacing perpendicular to the fracture plane ($h=0.5$ mm) but for different amplitudes of the lateral displacement ($\bigcirc$)$u=0.25$ mm; ($\square$)$u=0.5$ mm; ($\diamond$)$u=0.75$ mm; ($\triangle$)$u=1.2$ mm.

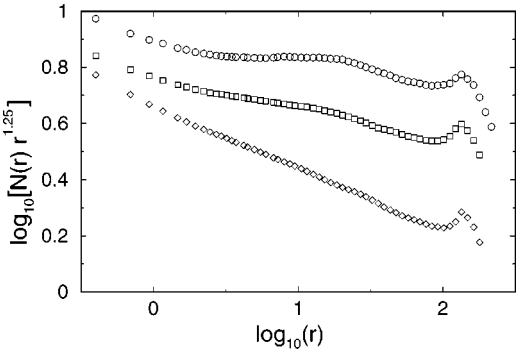

FIG. 9. Variation with the distance r (in mm) of the ratio $N(r)r^{-1.25}$ for a series of experiments performed at a same flow rate $Q=6.45$ ml/min and for a same lateral displacement $u=2$ mm. The mean normal spacing perpendicular to the fracture plane is $h=1.25$ mm, 1.5 mm and $h=1.75$ mm, respectively, for ($\bigcirc$), ($\square$), and ($\diamond$). In the three cases, the mean distance between the front and the injection point is 67 mm.

lower boundary r_m of the fractal domain remains close to 2.5 mm at injection times of 60 s and above; its value is however higher at the beginning of the experiment ($r_m=4$ mm for $t=30$ s). On the contrary, the upper boundary r_M increases markedly and continuously as predicted between 30 s and 180 s (by a factor of order 2). This variation is as expected of the same order of magnitude as that of the global size of the invaded zone: the latter increases roughly as the square root of time (corresponding to a factor of order $\sqrt{6}$ in the present case).

2. Dependence on the lateral shift

Figure 8 displays normalized curves similar to those of Fig. 6(b) corresponding to a same flow-rate and a same injection time but to different lateral displacements u ranging from 0.25 to 1.2 mm. The vertical translation $h=0.5$ mm between the surfaces is kept constant. The value $D=1.25$ that provides the best global adjustment at all u values has been used for all curves in this graph. Three of the curves display indeed clearly horizontal sections corresponding to the fractal domain. Only the curve obtained for $u=0.25$ mm has a small downwards slope in the fractal region; this part of the curve becomes horizontal when one uses instead the value $D=1.22$ that is only slightly lower than the value $D=1.25$ used for all other curves. This confirms again that the fractal dimension D does not depend on u. The lower limit r_m of this domain is always of order 2 mm and does not depend on the displacement u. It appears therefore to be controlled by the mean distance h between fractures that is of the same order of magnitude. The upper limit r_M of the fractal range, on the contrary, increases roughly as the square root of the displacement u.

3. Dependence on the mean aperture

Experiments where the normal relative displacement of the surfaces is varied while the lateral shift is kept constant were also performed. In this case, absolute fluctuations of the local aperture remain constant while their relative values with respect to the mean aperture h decrease as h increases. Figure 9 displays $N(r)$ variations obtained in a same fracture for various h values and for a lateral displacement $u=2$ mm and an injection flow rate that are both constant. Furthermore, the mean distance between the fronts and the injection point is the same for the three fronts studied and the value $D=1.25$ has been used for all curves. A clear constant part is only visible on the curve corresponding to $h=1.25$ mm. For $h=1.5$ mm and $h=1.75$ mm an horizontal section at intermediate length scales is only obtained, respectively, for $D=1.18$ and $D=1.1$. Moreover, the width of these sections decreases when h increases, both because r_m increases and r_M decreases ($r_M\approx 20$ mm and $r_m\approx 2.5$ mm for $h=1.25$ mm while $r_M\approx 14$ mm and $r_m\approx 3$ mm for $h=1.5$ mm). These results reflect the fact that the front appears smoother and smoother when h increases as can be seen on the pictures of Fig. 5. Since the value $D=1.1$ for $h=1.5$ mm is in addition very close to 1, a fractal description of the front is not therefore adequate for this experiment ($h=1.25$ mm represents then a transition case). The theoretical expectation is that larger apertures should still produce a similar scaling as small ones. However, the amplitude of the front roughness is expected to be reduced for a similar amount of injected fluid, and thus larger volumes are required to develop fully a fractal geometry.

D. Discussion of the results

A first important result of the previous analysis is the existence of a domain of length scales over which the front geometry can be considered as fractal. Various experiments performed with moldings of several granite samples indicate that the corresponding fractal dimension is $D=1.23\pm 0.05$. Moreover, this D value does not depend on the relative position of the two surfaces, on the injection time and on the flow rate (provided inertial or gravitational effects are negligible). This value of D is also in agreement with theoretical and numerical studies [9,8] predicting that $D=2-H$ for such processes in self-affine structures of characteristic exponent H. The corresponding value $H=0.77\pm 0.05$ is indeed

in agreement with the value found experimentally for our surfaces through direct profilometry measurements.

The lower limit r_m of the fractal domain varies little either with the lateral displacement or the injection time. It represents a lower cut-off length, reflecting the fact that geometrical features of the front markedly smaller than the local spacing are likely to be blurred out. The fractal characteristics of the front also disappear when the mean separation of the surfaces is not small any more compared to the aperture fluctuation (then, the apparent fractal dimension of the front decreases to 1). On the other hand, the upper cutoff of the fractal regime r_M increases significantly with the global front size and the lateral shift u. As could be expected, the width of the fractal domain vanishes out when the surfaces are just pulled apart $u=0$ (in this latter case, a smooth front is observed with only small scale irregularities).

IV. CONCLUSION

Experiments presented in this paper have demonstrated a possible relation between the multiple scale geometry of the invasion front between complementary rough fracture surfaces and the self-affine exponent of the surfaces. This front geometry reflects the disorder of the velocity field in the space between surfaces: it appears when the surfaces are displaced laterally from their contact position and when their mean spacing is not too large compared to the amplitude of the aperture fluctuations. When these conditions are met the front is fractal over a range of length scales that gets broader as the injection time and the lateral shift increase. Moreover, the same value $D=1.23\pm0.05$ of the fractal dimension is found for a large range of relative displacements and injected volumes: it appears to be directly related to the characteristic Hurst exponent $H=0.77\pm0.05$ of the self-affine geometry of the surfaces by $H=2-D$.

A key point is the robustness of these values with respect to variations of the experimental parameters: it results in part from the fact that only the outer boundary of the invasion front is analyzed. It is determined by the maximum velocity half-way between the surfaces and is not influenced by the parabolic velocity profile between them. On the other hand, this profile will induce Taylor dispersion due to the lower velocity of the injected fluids near solid surfaces. Such 3D effects will in turn influence other measurements such as that of the transit time distribution of fluid particles. Such measurements will therefore provide additional information on the flow distribution between the surfaces: they should however be realized in a parallel flow geometry (instead of the radial one used here) to avoid the effect of velocity variations with distance from the injection point. Using parallel flow will, in addition, allow using alternative methods to analyze the outer front geometry (e.g., tools adapted to self-affine curves). More information may also be obtained by replacing Newtonian fluids used in the present work by shear-thinning ones in order to enhance velocity contrasts between slow and fast flow regions: this should, in turn, enhance the fractal character of the front geometry.

Another important issue is the anisotropy of the shape of the invaded zone observed on some samples. This contrasts with the lack of dependence of average power spectra of surface profiles on their orientation. This anisotropy may depend both on the direction of the lateral displacement and on its orientation with respect to that of the fracture propagation. Such experiments may therefore represent a fruitful approach to detect and analyze anisotropies of fracture surfaces remaining un-noticed through conventional profilometry techniques.

Throughout this work we have assumed that the characteristics of the fracture surfaces were known and studied how the front geometry was related to them. Conversely, the knowledge of the invasion front geometry and of its dependence on the relative displacements of the fracture surfaces might provide useful informations both on the flow distribution between these surfaces and on their geometry.

ACKNOWLEDGMENTS

We are pleased to acknowledge useful discussions with D. Bideau, F. Cornet, G. Drazer, J. Koplik, Y. Meheust, J. Schmittbuhl, P.Z. Wong, and M. Zamora. We are indebted to S. Bourles for the realization of the fracture moldings and to O. Brouard, G. Chauvin, C. Saurine, and D. Vallet for that of the experimental setup. This work was partly supported by the ARC ''Géothermie des roches fracturées'' and the PNRN and PNRH-CNRS programs. This work was also supported by the CNRS and ANDRA through the GdR FORPRO (Research Action No. 99.VIII) and corresponds to the GdR FORPRO Contribution No. 2001/03 A. One of the authors (H.A.) thanks the GDR P.M.H.C. for a three months grant.

[1] S. Painter, S. Cvetkovic, and J. O. Selroos, Phys. Rev. E **57**, 6917 (1998).
[2] B. Berkowitz and H. Scher, Phys. Rev. Lett. **79**, 4038 (1997).
[3] P. Maloszewski, A. Herrmann, and A. Zuber, Hydrogeol. J. **7**, 209 (1999).
[4] J. Koplik, I. Ippolito, and J. P. Hulin, Phys. Fluids A **5**, 1333 (1993).
[5] G. Drazer and J. Koplik, Phys. Rev. E **62**, 8076 (2000).
[6] R. Gutfraind, I. Ippolito, and A. Hansen, Phys. Fluids **7**, 1938 (1995).
[7] V. V. Mourzenko, J. F. Thovert, and P. M. Adler, Phys. Rev. E **59**, 4265 (1999).
[8] F. Plouraboué, J. P. Hulin, S. Roux, and J. Koplik, Phys. Rev. E **58**, 3334 (1998).
[9] S. Roux, F. Plouraboué, and J. P. Hulin, Transp. Porous Media **32**, 97 (1998).
[10] S. Brown, A. Caprihan, and R. Hardy, J. Geophys. Res. **103**, 5125 (1998).
[11] A. Keller, P. Roberts, and M. Blunt, Water Resour. Res. **35**, 55 (1999).

[12] F. Plouraboué *et al.*, J. Contam. Hydrol. **46**, 295 (2000).
[13] Y. Méheust and J. Schmittbuhl, Geophys. Res. Lett. **27**, 2989 (2000).
[14] I. Ippolito, P. Kurowski, and J. P. Hulin, in *Fractured and Jointed Rock Masses*, edited by Myer, Cook, Goodman, and Tsang (Balkema, Rotterdam, 1995), pp. 527–533.
[15] J. Feder, *Fractals* (Plenum, New York, 1988).
[16] B. Mandelbrot, *The Fractal Geometry of Nature* (W. H. Freeman, New York, 1982).
[17] E. Bouchaud, G. Lapasset, and J. Planès, Europhys. Lett. **13**, 73 (1990).
[18] K. Måløy, A. Hansen, and E. L. Hinrichsen, Phys. Rev. Lett. **68**, 213 (1992).
[19] C. Poon, R. Sayles, and T. Jones, J. Phys. D **25**, 1269 (1992).
[20] W. Power *et al.*, Geophys. Res. Lett. **14**, 29 (1987).
[21] S. Brown and C. Scholz, J. Geophys. Res., [Oceans] **90**, 12 575 (1985).
[22] J. Boffa, C. Allain, and J. P. Hulin, Eur. Phys. J.: Appl. Phys. **2**, 281 (1998).
[23] H. Auradou *et al.*, Phys. Rev. E **60**, 7224 (1999).
[24] T. Anderson, *Fracture Mechanics*, 63 ed. (CRC Press, Boca Raton, FL, 1991).
[25] J. Schmittbuhl, J. P. Vilotte, and S. Roux, Phys. Rev. E **51**, 131 (1995).
[26] C. Poon, R. Sayles, and T. Jones, J. Phys. D **25**, 1269 (1992).
[27] *Handbook of Chemistry and Physics*, 63 ed., edited by D. Lide (CRC Press, Boca Raton, FL, 1983).
[28] G. Taylor, Proc. R. Soc. London, Ser. A **219**, 186 (1953).
[29] P. Kurowski (private communication).